Geophysical evidence for an active mantle plume underneath Elysium Planitia on Mars

In the format provided by the authors and unedited

This PDF file includes:

Supplementary Text 1: Mantle plumes and convective upwellings.

Supplementary Text 2: Gravity and topography investigations.

Supplementary Text 3: Plume-induced uplift in the highlands.

Supplementary Text 4: Additional discussion of loading and faulting on geologic timescales.

Supplementary Text 5: Plume head size, spreading, and cooling.

Supplementary Table 1: Parameter used for the different inversions.

Supplementary Figure 1: Plume shape, uplift, and stresses.

Supplementary Figure 2: Plume model long-wavelength fit to observed gravity and topography.

Supplementary Figure 3: Topographic maps of the craters shown in Figure 4.

Supplementary Figure 4: Plume-induced uplift in the southern highlands.

Supplementary Figure 5: Stress field before the plume arrival.

Supplementary Figure 6: Stress field, depth, and global contraction.

Supplementary Figure 7: Representative stress profile for Cerberus Fossae.

Supplementary Figure 8: Martian surface composition from Gamma Ray spectrometer data.

Supplementary Figure 9: Effect of the mantle plume on the crustal thickness at Elysium Planitia.

Supplementary Figure 10: Effect of the mantle plume on the crustal thickness at the InSight landing site for different plume properties.

Supplementary Figure 11: Geologic masks used for the crater counts.

Supplementary Text 1: Mantle plumes and convective upwellings.

Mantle plumes and convective upwellings are both dynamical flow patterns that result from the thermochemical evolution of a planetary body. Yet, not all upwellings are plumes, and both are significantly different in terms of physical characteristics and geological implications. Mantle upwellings are large-scale dynamical steady-state outcomes of a convecting mantle and are the counterpart to mantle downwellings, which together take part in the global convection circulation. The global mantle convection interacts and feedbacks with plate tectonics on Earth, allowing for heat exchanges between the deep interior and surface. Mantle plumes, however, are anomalously hot material originating in a thin thermal boundary layer from the deep mantle and are largely independent of the general advective circulation (though they can be influenced by it locally). Mantle plumes are thought to be at the origin of enormous flood basaltic plains and hotspots on Earth and other planetary bodies[35]. For that reason, mantle plumes significantly differ from mantle upwellings in term of dynamics and physical characteristics.

While some thermal evolution models do predict the presence of mantle upwellings underneath Tharsis and or Elysium Mons today[44], those upwellings should be considered as passive features rather than true mantle plumes. They are caused by the presence of a thick crust rather than being the cause of it. The predicted upwelling is a result of the insulating effect and heat producing elements in the crust that warm the underlying mantle, thereby reducing the viscosity and facilitating upwelling there. As noted in the main text, volcanism in Elysium Planitia is distinct in space and time from volcanism at Elysium Mons and is not consistent with the thermal insulating effect of that edifice.

Supplementary Text 2: Gravity and topography investigations.

The gravity field at Elysium Planitia is strongly affected by the nearby Tharsis volcanic province, and to a lesser extent by the Elysium Mons volcano. In order to limit the contribution from neighboring features, most studies of gravity, topography, and lithospheric loading have opted for an efficient spatio-spectral localization technique[25,63]. This approach, however, does not work here, as the wavelength associated with the mantle plume's signal (4000 km or spherical harmonic degree 3), largely overlaps with that associated with both Tharsis and Elysium Mons[25] (up to degree ~10). The spatial region of interest also overlaps with Tharsis (whose effects are global) and Elysium Mons (at the northwest margin of the plume-induced uplift, Fig. 2). For those reasons, it is not possible to design a localization window that both removes Tharsis and Elysium Mons' signatures and preserves a local unbiased long-wavelength plume signal. Alternatively, filtering or masking procedures could have been applied to gravity and topography to limit Tharsis and Elysium Mons' contributions to the local field. However, we found that these also affected our wavelengths of interest and introduced significant ringing in the Elysium Planitia region. We thus conclude that standard localization, masking, or filtering techniques are not suitable for our analysis. Finally, we also tested models in which we subtracted forward models of Tharsis and Elysium Mons from observed gravity and topography, but this was not found to be effective and required a number of poorly constrained assumptions.

For those reasons, we opted for a simpler approach and investigate north-south profiles in Elysium Planitia that parallel the circum-Tharsis trough. Given the symmetric circular nature of the Tharsis trough (largely an effect of the membrane support of the load and the resulting degree-one center-of-mass-center-of-figure offset), profiles that parallel the trough will be little affected by its signal.

The profiles were also taken sufficiently far (1200 km away) from Elysium Mons to be unaffected by the flexural signal around that load (~650 km). The extracted profiles will thus be representative of Elysium Planitia's geophysical signature, and can be used to characterize the plume signature. We note that similar gravity profile investigations have been done extensively in regions with complicated gravity field or load geometries[64,65].

Nevertheless, we acknowledge that the plume-induced signal in the gravity data is difficult to disentangle from the regional effects of Tharsis. It is important to note that by virtue of Mars' radius and lithospheric strength, loads are largely supported by the lithosphere, changing the characteristic signature of a mantle plume relative to one on a planet with a larger radius and/or thinner lithosphere. This draws one important difference between Mars and Venus, where the large radius and weak lithosphere on the latter cannot support long-wavelength loads, thus allowing for diagnostic gravity and topography signatures of mantle plumes[23]. In contrast, on Mars it is possible to show that gravity and topography are consistent with a mantle plume, but mantle support of topography is not required and non-unique since lithospheric support of topography cannot be ruled out at any scale. Despite these difficulties, we emphasize that the observed gravity signal does match the expectations for a mantle plume, and that the plume hypothesis is strongly supported by independent evidence from topography, tectonics, and the volcanic history. As a simpler, but less rigorous, test of the plume hypothesis, we also note that while the topography in Elysium Planitia is higher than the rest of the northern lowlands, the crust is not proportionally thicker and thus the high topography cannot be explained as reflecting isostatic crustal thickening of unknown cause.

Using our thin shell model, we have inverted the long-wavelength gravity and topography of Elysium Planitia for the plume and lithosphere parameters (Fig. 2, Methods). The elastic thickness of the lithosphere is poorly constrained in our inversion for several reasons (Supplementary Figure 2). In some cases, the wavelength dependence of the gravity and topography can be used to constrain lithosphere thickness (either in the form of an admittance spectrum or a spatial fit to the data). In this case, the diameter of the uplifted region of ~4000 km corresponds to the half-wavelength at spherical harmonic degree 3. At this wavelength, lithospheric support is dominantly by membrane stresses[66]. For example, in the degree-range of 2 to 5, the degree of compensation is nearly independent of degree and only weakly dependent on lithosphere thickness varying from ~0.73 to ~0.55 for thicknesses between 75 and 150 km. Because the magnitude and wavelength of the load itself are not independently constrained, the gravity and topography only weakly constrain the lithosphere thickness. Particularly thick lithospheres (>400 km) can be excluded as not matching the gravity and topography, but a broad range of lithosphere thicknesses (25–200 km) provide reasonable fits to the data when taking into account tradeoffs with the magnitude and size of the load.

We ran an additional model in which we inverted the topography of the entire Elysium Planitia region after having masked Elysium Mons and the highlands south of the dichotomy, rather than the two orthogonal profiles. For this inversion, we found the same best-fit parameters as our profile-based topography inversion described above. This indicates that Elysium Mons is not affecting our inverted parameters and that our inversion based on a few profiles is robust.

Supplementary Text 3: Plume-induced uplift in the highlands.

Given that a plume-induced uplift is visible in both the crater floors and long-wavelength signature of the northern lowlands, a similar uplift should also be visible directly south of Elysium

Planitia, within the southern highlands. We have investigated surface elevations in the southern highlands using radial profiles from our inferred best-fit plume head center (160°E, 7.5°N) to a distance of 4000 km (Supplementary Figure 4a). The average profile reveals a long-wavelength signal consistent with our plume-induced uplift, for the same parameters as used in Fig. 1 (Supplementary Figure 4b). The large (> 1000 km) Hesperia Planum (105°E, 20°S) stands out from the southern highlands as a topographic low, and we thus performed a similar investigation of plume uplift excluding this region (Supplementary Figure 4c). Although this slightly modified the average profile, a long-wavelength signal consistent with a plume-induced uplift is still present (Supplementary Figure 4d). We must, however, acknowledge the relatively high standard deviation associated with the roughness of the southern highlands compared to that of the lowlands, where a clear plume-uplift signal was detected (Fig. 2).

Supplementary Text 4: Additional discussion of loading and faulting on geologic timescales.

The vast majority of Mars' volcanically-induced crustal loading occurred during the first 1.5 billion years of its geologic history[1,3] (Fig. 1). Owing to the absence of lithosphere recycling, the planet's geodynamical response to these loads is kept frozen within the mechanical memory of the lithosphere as Mars cooled over time. These signatures can be revealed by inverting gravity and topography for the associated displacement and loads (Methods).

We consider two different scenarios for modeling the stress field, as described in the main text: one in which stresses arise only from crustal loading as predicted by the inversion of present-day gravity and topography, and one in which we include the effects of a mantle plume. For the second scenario, the stress field in the Cerberus Fossae region, before the plume arrival, is initially compressive throughout the lithosphere (Supplementary Figures 5d and 7). The plume-induced uplift is however able to place the lithosphere in extension at all depths except for a shallow and relatively thin compressional zone from 3 to 18 km (Supplementary Figures 6 and 7, depending on the amount of added global contraction). This is a result of the specific sequence of flexural loading, global contraction, and plume induced-uplift assumed, together with the limiting of the stresses by the yield strength envelope, and can be explained as follows. Before both plume arrival and global contraction, the ancient Tharsis-induced extension at Elysium Planitia exceeded the yield strength and generated extensional failure down to a depth of about 35 km (Supplementary Figures 5c and 7). Global contraction then overcame all ancient extension, placing the lithosphere in compression and triggering wrinkle ridge formation (Supplementary Figure 5d). The associated crustal failure released stresses exceeding the yield strength down to 7 km depth. Between 7 and 35 km depth, the vertical stress profile still follows the extensional yield strength envelope but is shifted into the compressional domain by the contractional stresses. Below 35 km depth, the yield strength was never exceeded, and the extensional stresses from Tharsis and compressional stresses from global contraction approximately cancel. The arrival of the plume-induced tensile stresses (~50 MPa, Supplementary Figure 1) then pushed the lithosphere into extension except for a shallow compressive zone at 3–18 km depth where post-contraction compressional stresses exceeded the plume-induced extension (Supplementary Figure 7). We note that, aside from steep stress gradients arising from the imposed frictional yield strength envelopes, stresses are relatively constant through the lithosphere. These uniform stresses are because the lithospheric support of both Tharsis and the Elysium plume are dominated by membrane effects, and there are no major short-wavelength loads supported by bending stresses in the area of interest. The specific vertical variations in the stress field are sensitive to the model assumptions, as explored below, but the

result that plume-induced uplift is required to overcome the net effect of regional loading and global contraction is robust.

An alternative approach to the loading and contraction scenario detailed in the main text would consider that ancient crustal loading operated in parallel to global contraction and crustal failure. In this scenario, the volcanically-induced stresses would be partly counterbalanced by planetary contraction prior to failure and limited by the yield strength. Variations in the relative rates and timing of Tharsis' loading (which dominates the early stress field) and global contraction would affect only the stresses in the shallow lithosphere, where stresses exceeded the compressional yield strength (~7 km depth, Supplementary Figure 7). In our dike models, all of the non-eruptive dikes are confined below this depth (> 15 km) and would be little affected. Nevertheless, a component of the global contraction in parallel with the Tharsis-induced extension would result in a less compressional shallow lithosphere (as more of the Tharsis stresses were able to counteract the contractional stresses), allowing dikes to erupt to the surface for lower magma pressures. This, however, does not affect the key results or interpretations of this study. The specific timing and rates of Tharsis' construction and global contraction are uncertain. However, given that the primary evidence for global contraction are the pervasive wrinkle ridges on Hesperian surfaces, including those surfaces at the top of the Tharsis load itself[3], a large component of the contractional stresses must post-date the bulk of Tharsis.

We note that although some constraints exist on the tectonic and loading history of Mars, mostly dominated by Tharsis[67], and the time evolution of global contraction[7,68], any retrieved time-evolution of the stress field will be subject to significant uncertainties. Below, we consider one simple scenario to provide a first-order estimation of the outcome. Given that Tharsis has dominated the global crustal stress field, we assume that the loading history is reflected in Tharsis' tectonic history (represented by the number density of faults of a given age). Based on an analysis of Tharsis tectonics[67], we assume that 33% of Tharsis formed in the Noachian (prior to any substantial global contraction), 57% of Tharsis formed in the Hesperian (in parallel with the bulk of global contraction), and 10% of Tharsis formed in the Amazonian (after the main phase of global contraction). We take these values as a proxy for the evolution of the global Martian stress field. These values are used together with crustal failure and a time-variable global contraction from a parameterized convection model[7,68], to integrate the stress evolution. For this assumed time-evolution sequence, we obtain tensile stresses of 180 MPa at 20 km depth and at the end of Tharsis' construction (in comparison to 300 MPa for the original scenario of Tharsis loading prior to any global contraction). Both scenarios result in extensional stresses higher than the crustal yield strength in extension at all depths less than 25 km, such that the stresses after limiting by the yield strength and the addition of any later contraction would be identical. Based on our estimated present-day stress profile (Supplementary Figure 7), any depth deeper than 35 km also would not be affected, as stresses at these depths never exceeded the yield strength in extension or compression and thus these depths preserve a perfect record of the net stress independent of the time history.

Thus, we conclude that both shallow (<25 km) and deep (>35 km) depths are little affected by the specific time history of loading and contraction, for different reasons. The stress at intermediate depths (~25–35 km) does depend on the assumed sequence of Tharsis loading, global contraction, and lithospheric failure to limit stresses to the yield strength. A model with global contraction occurring in parallel with Tharsis formation will increase the extensional stresses in this intermediate zone and favor dike and fissure formation. The specific dike cross-sections, the

vertical extents of the dikes, and the magma pressure required for eruption and fissure formation at the surface are all affected by the vertical stress profile. However, for any scenario there will be a tendency for dikes to intrude below the level of the compressional stresses predicted in the shallow lithosphere.

Supplementary Text 5: Plume head size, spreading, and cooling.

Several parameters influence the diameter of a plume head in the mantle (D), including the rise height through the mantle (Z), the kinematic viscosity (v), and the gravitational attraction (g), which all are expected to differ between the Earth and Mars, where[29,69]

$$D \propto Z^{3/5}(v/g)^{1/5}.$$

On Earth, plume heads are predicted to have diameters ranging from 1000–1200 km in the mantle (with a viscosity of 10^{20} Pa s), and flatten at the base of the lithosphere to reach diameters of 2000–2400 km (refs.[24,29,69]). Importantly, the Martian mantle viscosity is estimated to be higher than on Earth, with values ranging from 10^{21} to 10^{22} Pa s (refs.[43,44]). The higher viscosity is likely the result of the Martian mantle being relatively dry compared to Earth in which the mantle is constantly hydrated by crustal recycling[42]. On Mars, for a plume coming from the core-mantle boundary, assuming a constant mantle viscosity of 10^{21-22} Pa s (refs.[43,44]), the equivalent plume heads would have diameters of 1600 to 2550 km in the mantle, and 3200 to 5100 km after flattening. Our model results are thus consistent with expected plume head sizes on Mars.

During the ascent in the mantle, the plume head rises at a speed of[69]

$$U = g \, \alpha \, \Delta T \, D(t)^2/12v,$$

where α is the mantle thermal expansivity, ΔT is the plume temperature anomaly, and $D(t)$ denotes the plume diameter at a given time. We assume a plume head diameter of 2000 km, before flattening and temperature anomaly of 175 K, consistent with our results at Elysium Planitia, a thermal expansivity of 3×10^{-5} K^{-1} (ref.[44]), and mantle viscosity of 10^{21-22} Pa s (refs.[43,44]). The resulting ascending velocity is expected to be about 0.07–0.7 m/year, which is one to two orders of magnitude lower than on Earth[29,69], where we obtain 7 m/year assuming a viscosity of 10^{20} Pa s and plume diameter of 1200 km.

On Earth, the typical spreading timescale of a mantle plume is about 5–20 Myr (refs.[29,69,70]) for an upper mantle viscosity of 10^{20} Pa s (velocity of ~0.1–0.4 m/year), and volcanism has been observed to last 1–10 Myr. Owing to the higher predicted mantle viscosity of 10^{21-22} Pa s, the spreading timescale on Mars is expected to last 50 to 2000 Myr, for a duration of volcanism of ~10–1000 Myr. This timescale is consistent with the observed relatively long duration of volcanism at Elysium Planitia (~125 Myrs). We also note that geologic observations suggest that Elysium Planitia's volcanism occurred during two major pulses[10,19,38] (at ~30 and 125 Ma), consistent with pulsed activity in terrestrial large igneous provinces[35].

The characteristic cooling timescale of a plume head can be estimated from Fourier's law of heat conduction in 1-D to be $\Delta t \sim L^2/\kappa$, where κ is the thermal diffusivity of the media and L is a characteristic length. For a plume in the mantle with diffusivity of 10^{-6} m^2 s^{-1}, located underneath a 150-km thick thermal lithosphere[44], the diffusive timescale is 713 Ma, which exceeds the minimum spreading and advection timescale.

6

Together, these estimates imply that Martian plume heads will be larger and longer-lasting, and result in lower rates of volcanism, when compared to those on Earth.

Supplementary Table 1: Parameters used in the different inversions.

Inversion, Figure display	Elastic thickness, km	Plume radius, km	Plume aspect ratio (thickness, km)	Plume density anomaly, kg m^{-3}	Crustal density, kg m^{-3}	Crustal thickness, km
Plume uplift, Figure 2	150	2000	0.08 (320)	-20	2800	50
Stresses without plume, Figure 5A	100 [Tharsis stresses]	–	–	–	2800	50
Post plume stresses, Figure 5B and C	100 [Tharsis stresses] 150 [Plume stresses]	2000	0.08 (320)	-20	2800	50
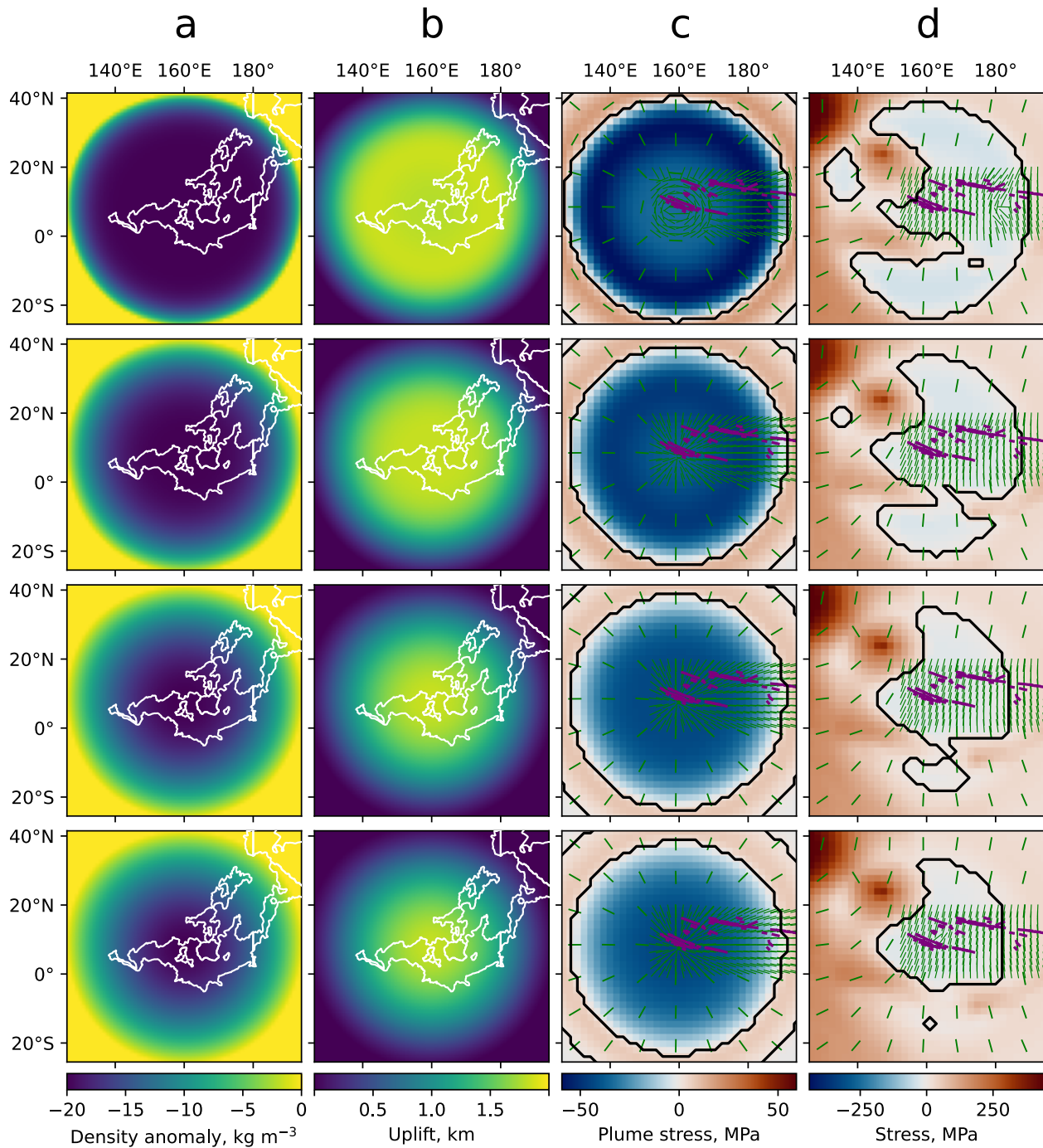
Supplementary Figure 1: Plume shape, uplift, and stresses. Influence of the tapering of the plume head density contrast or shape (a) on the surface uplift (b), and on the most tensile horizontal stress for the plume only model (c) and for the model including crustal loading, contraction, and the plume (d, similar to Fig. 5B). Positive stresses indicate compression and the black line in c and d indicates where stresses are zero. Our nominal model is that on the second row. As in the main text, the stress field in (d) is limited by the crustal yield strength at 20 km depth and overprinted by 160 MPa of global contraction before the plume arrival. The models taper the density contrast as the thickness of the plume cannot be tapered given our formulation. From bottom to top, the

radial distribution of the plume head density contrast (or temperature anomaly) ranges from a conical to a cylindrical shape. The (c) and (d) columns are similar to Fig. 5 in the main text, where purple lines annotate the Cerberus Fossae, and the green lines indicates the principal stress angle which should be orthogonal to the fossae. The radial spread of the density anomaly causes the central uplift to flatten (b), the extensional stresses to increase radially, and the most extensional stress to switch from radial to circumferential in the central region (c-d). However, all models predict similar stress orientations at Cerberus Fossae when added to the crustal loading stress field (d).
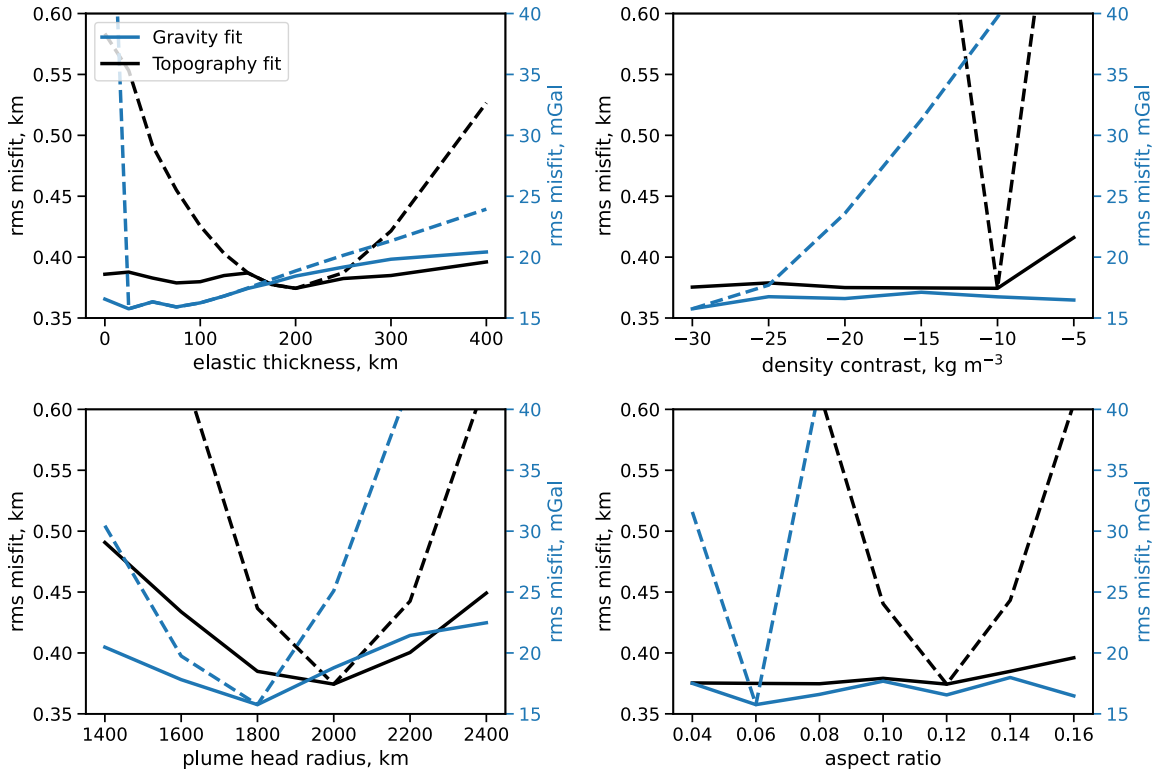
Supplementary Figure 2: Plume model long-wavelength fit to observed gravity and topography. Minimum root mean square (rms) misfit to observed topography (black) and gravity (blue) as a function of the elastic thickness (a), the plume head density contrast (b), radius (c), and aspect ratio (d). Solid lines give the misfit as a function of one parameter (x-axis) along the minimum misfit for all parameters, and the dashed lines give the best-fit as a function of one parameter while holding all others constant at their best-fit values. Best-fit elastic thicknesses are 25 and 200 km, density contrasts are -30 and -10 kg m^{-3}, radii are 1800 and 2000 km, and aspect ratios are 0.06 and 0.12, for gravity and topography fits, respectively. These aspect ratios imply plume thicknesses of about 220 to 480 km. We note that tradeoffs are expected between the aspect ratio and density contrast, which both control the plume head load magnitude. Assuming a mantle density of 3500 kg m^{-3} and a thermal expansivity of 3×10^{-5} K^{-1}, the inverted density contrast implies a temperature anomaly of 95 to 285 K.
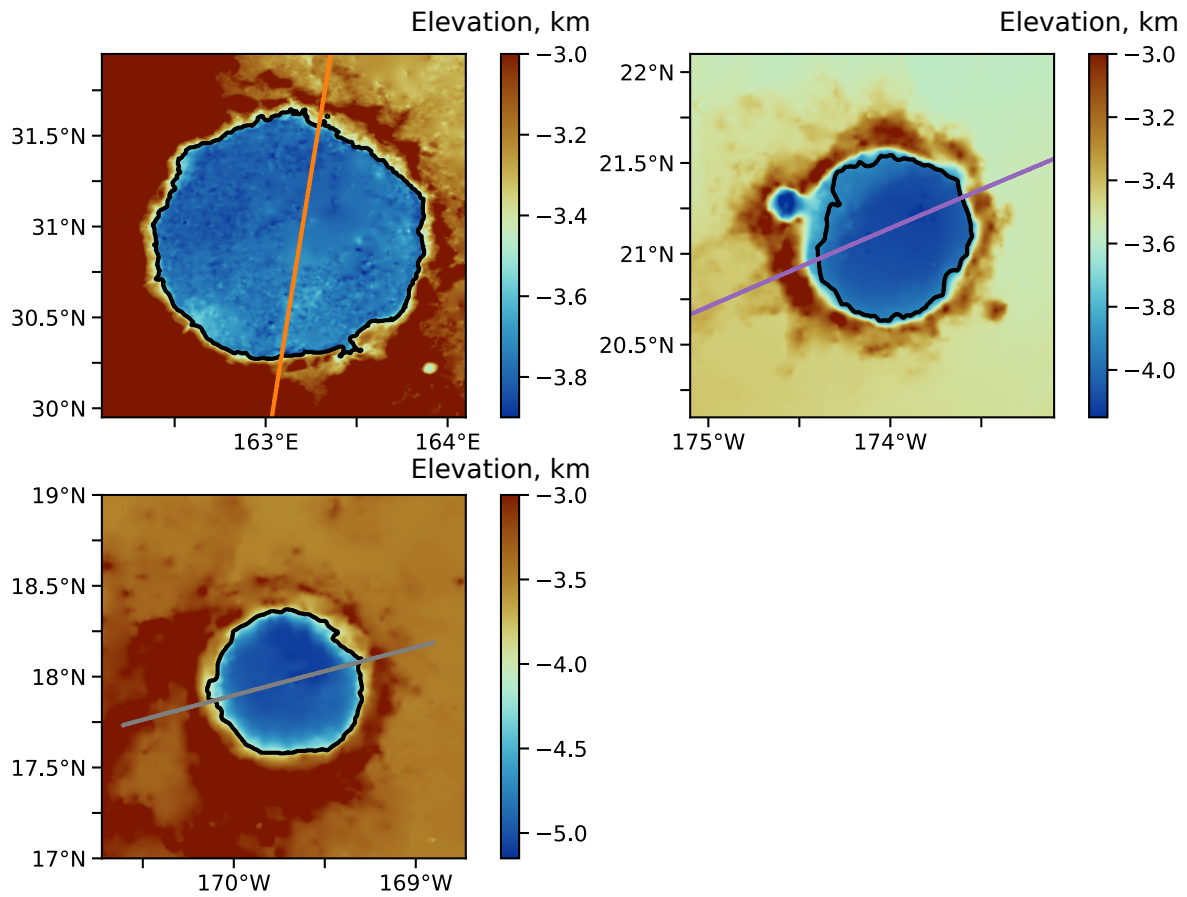
Supplementary Figure 3: Topographic maps of the craters shown in Figure 4. The colored line indicates the profile shown in Figure 4 of the main text, and the black contour displays the elevation-based mask that was used to extract the crater floor before finding the 3-D plane.
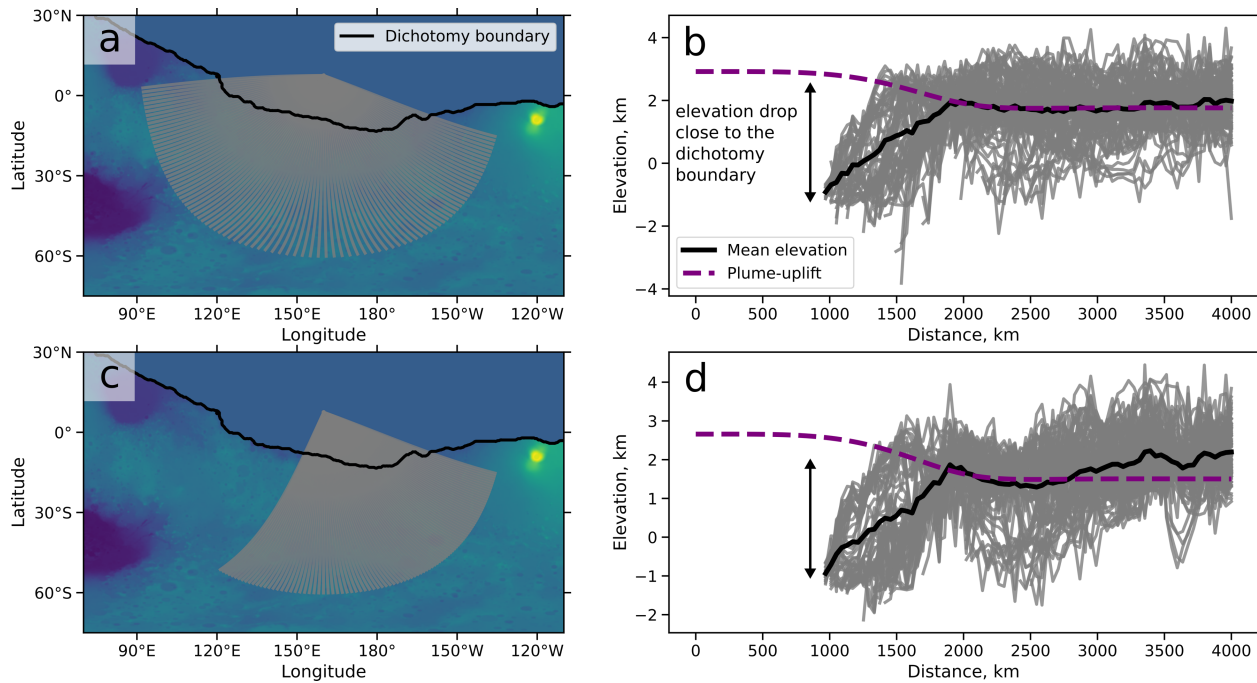
Supplementary Figure 4: Plume-induced uplift in the southern highlands. (a) Elevation map showing radial profiles (grey) from the plume head center to a distance of 4000 km, where the black line shows the dichotomy boundary. (b) Elevation profiles (grey) and average (black), excluding the lowlands, compared to our best-fit plume-induced uplift (purple). (c-d) Same as (a-b), but excluding the low-relief Hesperia Planum (105°E, 20°S). For both cases, a long-wavelength (>500 km) uplift is observed within the rough southern highlands and is consistent with our nominal plume model. However, we note the high uncertainties in the derived average profile given the large variability in surface elevations in the southern highlands. The drop in elevation at distances <1900 km is a result of the dichotomy boundary, which is intersected at different locations in different profiles.
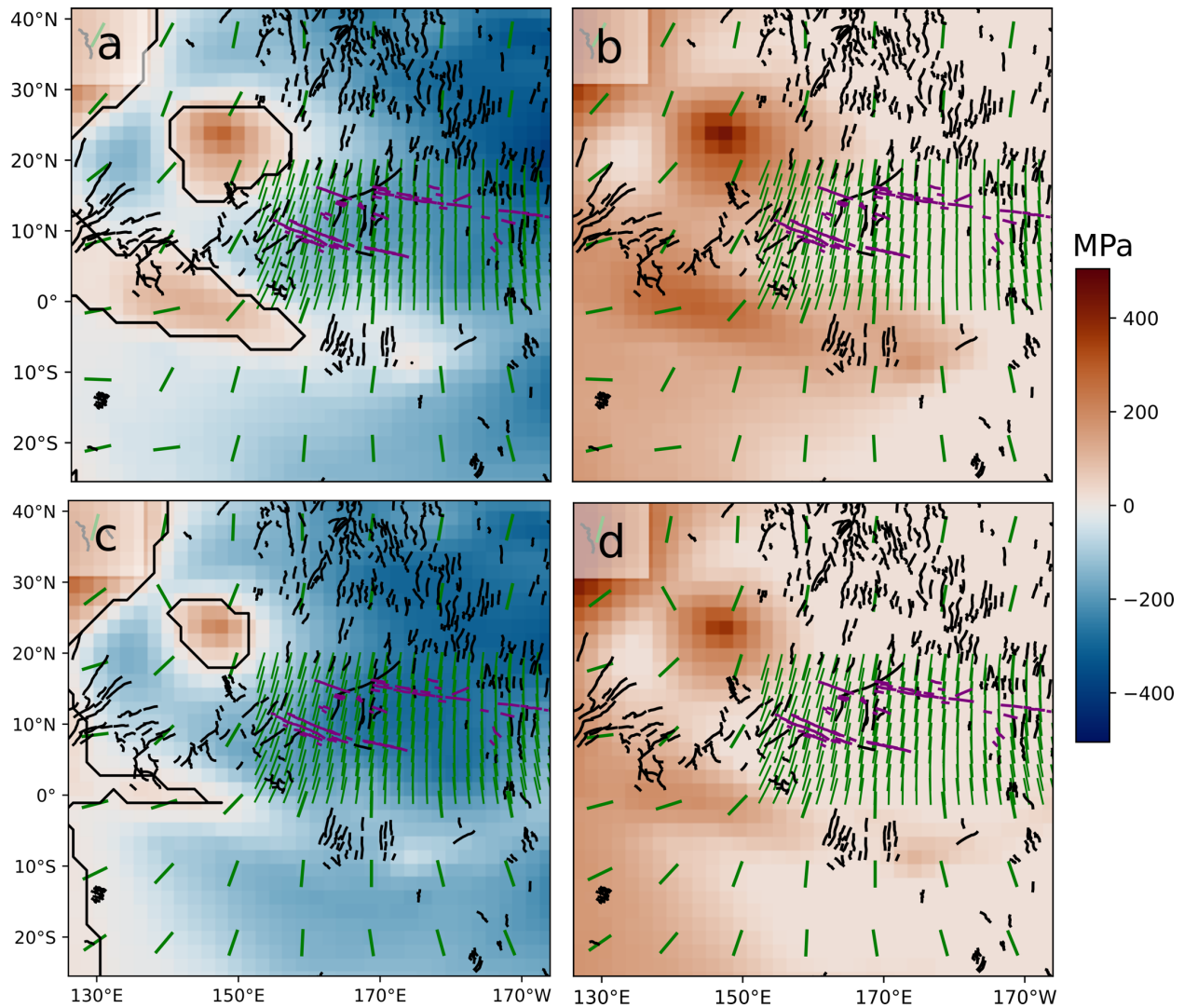
Supplementary Figure 5: Stress field before the plume arrival. (a) Stress field at 20 km depth under the assumption of crustal loading, with the Cerberus Fossae and wrinkle ridges annotated in purple and black, respectively. The black contour line indicates where the stresses are zero. (b) Same as (a), but where the stress field is limited by the crustal yield strength, overprinted by 160 MPa of planetary contraction. Planetary contraction exceeds the yield strength and forms wrinkle ridges, consistent with observations (Fig. 4 in the main text). (c) Same as (a), but where we have removed the plume signals from observed gravity and topography, before inverting for the crustal loading-induced stresses. (d) Same as (c), but where the stress field is limited by crustal failure and overprinted by global contraction, in order to show the stress field before plume arrival. The green lines indicate the principal stress direction.
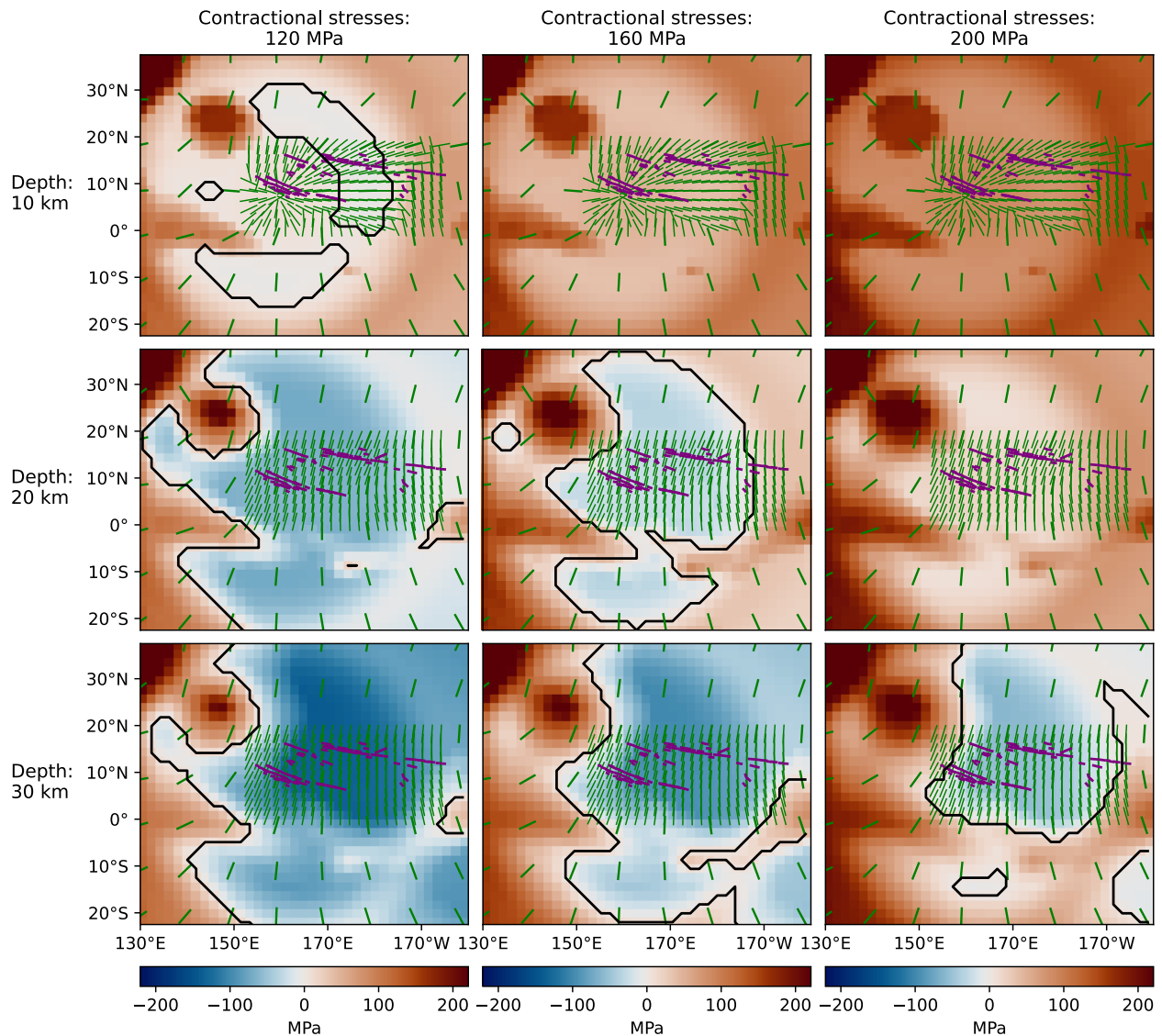
Supplementary Figure 6: Stress field, depth, and global contraction. Influence of the depth (rows, 10–30 km) and global contractional stress (columns, 120–200 MPa) on the modeled stress field magnitude and direction after the plume arrival (as shown in Fig. 5B). Increasing the global contractional stress (left to right) is seen to limit the regional extension. As depth decreases (bottom to top), extension also becomes limited, and the stress field is seen to become weakly compressional at 10 km depth (a few tens of MPa). This is due to the pre-plume arrival stress field being limited by a weak crustal yield strength, which is then overprinted by global contraction up to a value larger than the plume-induced stresses at that depth. However, we note that once a dike starts to propagate at depth where we predict extension, magma pressure at the dike tip will allow it to propagate in a relatively weak compressional field (Fig. 5C), as long as magma pressure overcomes the ambient stress field.
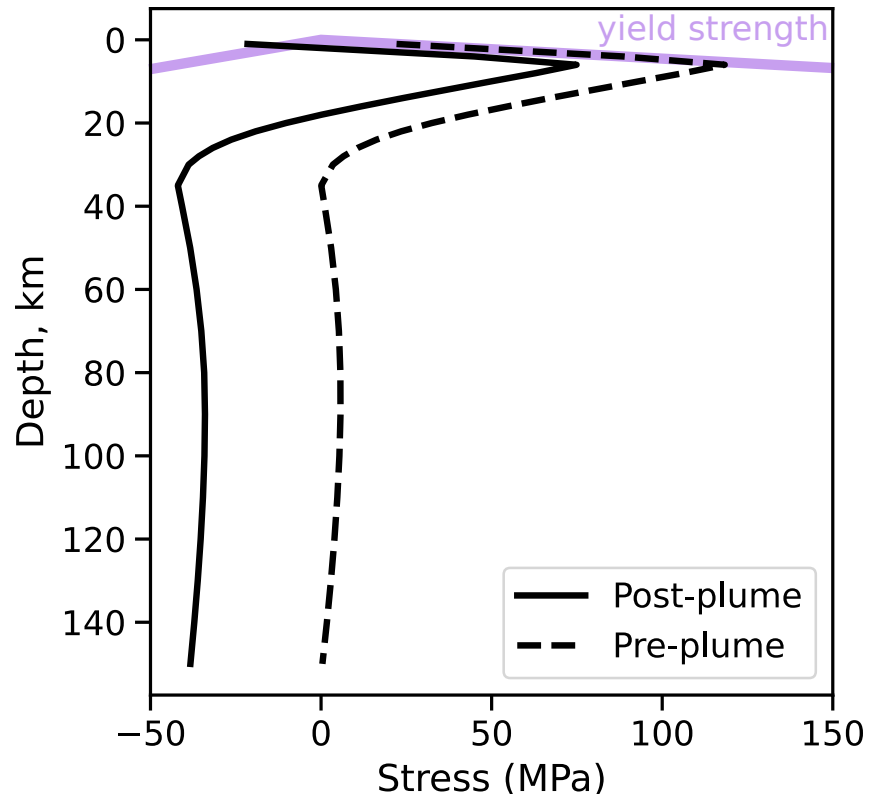
Supplementary Figure 7: Representative stress profile for Cerberus Fossae. Stress profile representative of Cerberus Fossae before (dashed) and after (solid) plume arrival (Methods), with the brittle yield strength being shown in purple. The profile represents an average stress over a 10° box centered on Cerberus Fossae (160°E, 7.5°N), which is our best-fit plume head center location. We note that given the long-wavelength of both the Tharsis and plume loads, membrane stresses dominate, which explains a relatively constant stress profile with depth where the yield strength has not been exceeded.
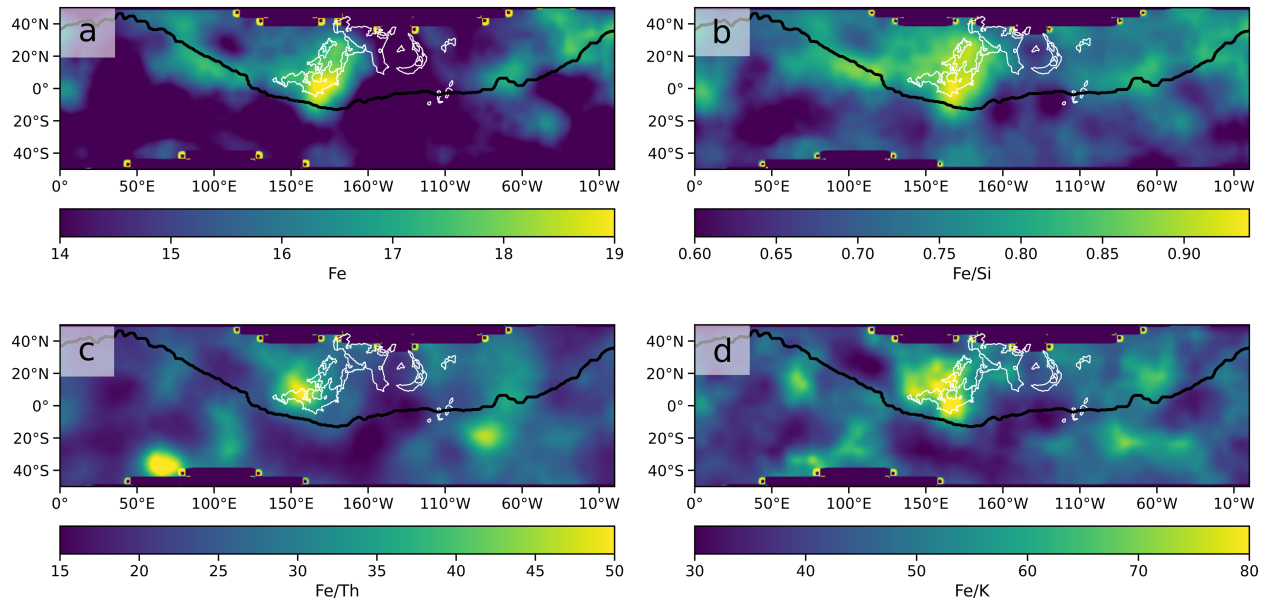
Supplementary Figure 8: Martian surface composition from Gamma Ray spectrometer data. Gamma Ray spectrometer elemental abundance maps[36] for Fe (a), Fe/Si (b), Fe/Th (c), Fe/K (d). The white lines indicate the Late Amazonian volcanics, and the black line indicates the dichotomy boundary. A clear relative enrichment in all quantities correlates with the extent of Elysium Planitia. Note that there is no Gamma Ray spectrometer data poleward of ~40°.
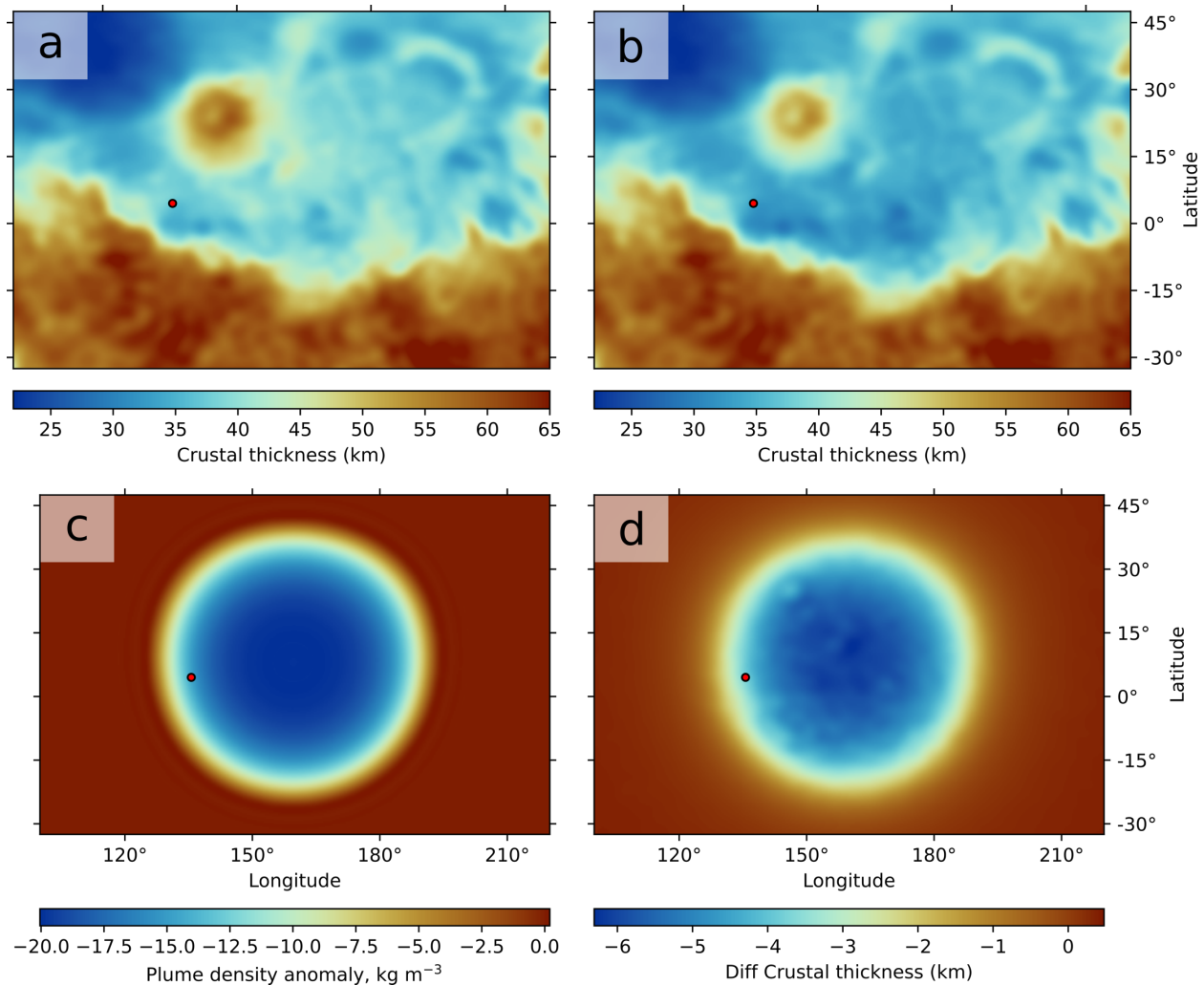
Supplementary Figure 9: Effect of the mantle plume on the crustal thickness at Elysium Planitia. (a) Crustal thickness inverted from observed gravity and topography assuming a crustal density of 2800 kg m^{-3} and thickness of 50 km. (b) Crustal thickness inverted from observed gravity and topography corrected for our nominal plume head model, with a density anomaly of 20 kg m^{-3}, diameter of 4000 km, and located between 150 and 470 km depth (thickness of 320 km). (c) Extent of the plume head density anomaly. (d) Crustal thickness difference between (a) and (b), where negative differences indicate a thinner crust for the plume model (b). For the full range of accepted plume models, the crustal thickness difference ranges from -3 to -11 km. The red dot indicates the position of the InSight lander, where the crust is 3.75 km thinner for the plume model (see Supplementary Figure 10).
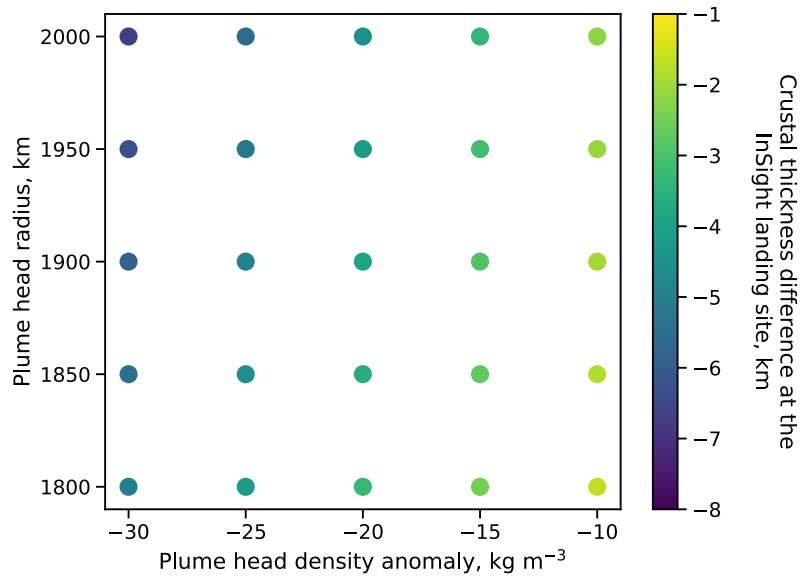
Supplementary Figure 10: Effect of the mantle plume on the crustal thickness at the InSight landing site for different plume properties. Crustal thickness difference at the InSight landing site for models with and without a plume underneath Elysium Planitia (Supplementary Figure 9), as a function of the plume head density anomaly and radius. The crustal density and thickness are set to 2800 kg m⁻³ and 50 km, respectively. The aspect ratio of the plume head and elastic thickness of the lithosphere have been set to 0.08 and 150 km, respectively. Given that gravity and topography crustal thickness models exactly fit the seismic constraint at the InSight landing site[20], the effects of the plume translate into an overestimation of Mars' global crustal thickness by ~1.5 to 6.5 km.
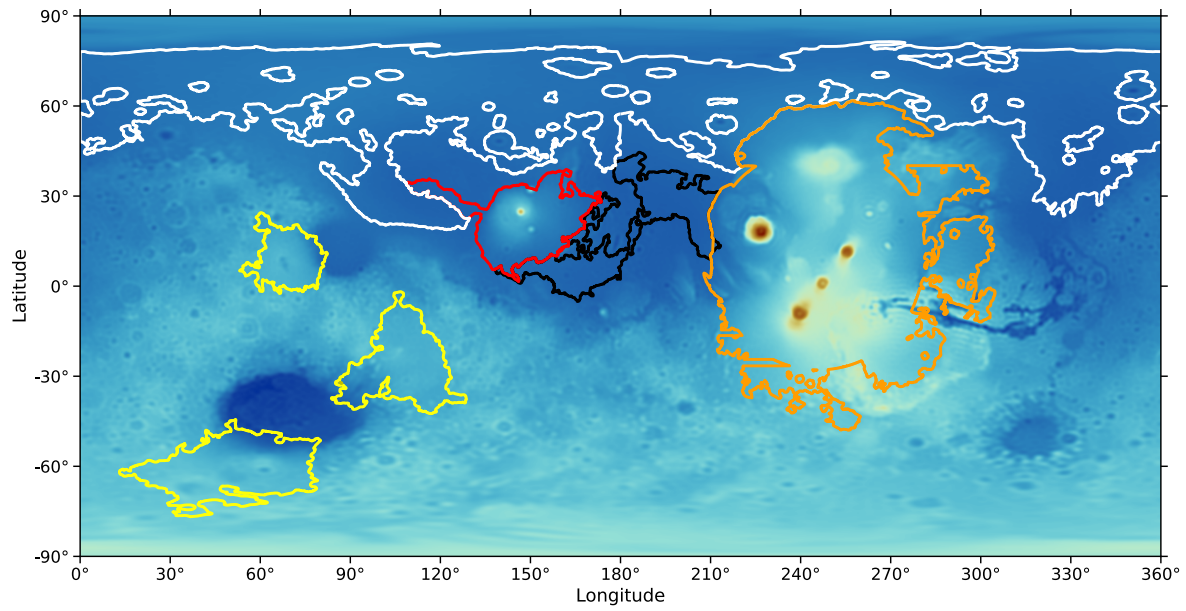
Supplementary Figure 11: Geologic masks used for the crater counts. Geologic masks based on geologic contours [3] for Elysium Mons (red), Elysium Planitia (black), the northern lowlands (white), Tharsis (orange), and the Hesperian highland volcanic provinces (yellow).

References:

[63] Wieczorek, M. A., & Simons, F. J., Localized spectral analysis on the sphere. *Geophys. J. Int.* **162**, 655–675 (2005). doi: 10.1111/j.1365-246X.2005.02687.x.

[64] Kiefer, W. S., Buried mass anomalies along the hemispheric dichotomy in eastern Mars: Implications for the origin and evolution of the dichotomy. *Geophys. Res. Lett.* **32**, L22201 (2005). doi:10.1029/2005GL024260.

[65] Andrews-Hanna, J. C. et al. Structure and evolution of the lunar Procellarum region as revealed by GRAIL gravity data. *Nature* **514**, 68–71 (2014). doi: 10.1038/nature13697.

[66] Turcotte, D. L., Willemann, R. J., Haxby, W. F., & Norberry, J., Role of membrane stresses in the support of planetary topography. *J. Geophys. Res.*, **86(B5)**, 3951–3959 (1981). doi: 10.1029/JB086iB05p03951.

[67] Bouley, S., Baratoux, D., Paulien, N., Missenard, Y., & Saint-Bézar, B., The revised tectonic history of Tharsis. *Earth Planet. Sci. Lett.* **488**, 126–133 (2018). doi: 10.1016/j.epsl.2018.02.019.

[68] Hauck, S. A., & Phillips, R. J., Thermal and crustal evolution of Mars. *J. Geophys. Res.* **107(E7)**, (2002). doi: doi:10.1029/2001JE001801.

[69] Griffiths, R. W., & Campbell, I. H., Implications of mantle plume structure for the evolution of flood basalts. *Earth Planet. Sci. Lett.* **99**, 79–93 (1990). doi: 10.1016/0012-821X(90)90072-6.

[70] Farnetani, C. G., & Richards, M. A., Numerical investigations of the mantle plume initiation model for flood basalt events. *J. Geophys. Res.* **99(B7)**, 13813–13833 (1994). doi: 10.1029/94JB00649.